There may be differences between this version and the published version. You are advised to consult the publisher's version if you wish to cite from it.

http://eprints.gla.ac.uk/229132/

Deposited on 26 January 2021

Origin of the Contact Force-Dependent Response of Triboelectric Nanogenerators

Guanbo Min[a,c], Yang Xu[a,b], Peter Cochran[a,b], Nikolaj Gadegaard[b], Daniel M. Mulvihill[a]* and Ravinder Dahiya[c]*

[a]Materials and Manufacturing Research Group, James Watt School of Engineering, University of Glasgow, Glasgow, G12 8QQ, UK

[b]Division of Biomedical Engineering, James Watt School of Engineering, University of Glasgow, Glasgow, G12 8LT, UK

[c]Bendable Electronics and Sensing Technologies (BEST) Group, James Watt School of Engineering, University of Glasgow, Glasgow, G12 8QQ, UK

ABSTRACT

Triboelectric nanogenerators (TENGs) have attracted significant interest as the alternative source of renewable energy. Their performance is believed to depend on the contact force, but its origin is yet to be established. Herein, we show that the origin lies in the *real* contact area A_r, probed with novel experiments specifically designed for this purpose. The open circuit voltage V_{oc}, short circuit current I_{sc} and A_r for a TENG, having two nominally flat tribo-contact surfaces, were found to increase with contact force/pressure. The A_r is notably small at low pressures (0.25% at 16 kPa) that are typically experienced in wearable applications. However, it increases 328 fold to as much as 82% when it saturates beyond about 1.12 MPa pressure - achievable for impact with ocean waves. Critically, V_{oc} and I_{sc} saturate at the same contact pressure as A_r suggesting that electrical output follows the evolution of the A_r. Assuming that tribo-charges can only transfer across the interface at areas of real contact, it follows that an increasing A_r with contact pressure should produce a corresponding increase in the electrical output. These results underline the importance of accounting for real contact area in TENG design to boost their performance, the distinction between real and nominal contact area in tribo-charge density definition, and the possibility of using TENGs as a self-powered pressure/load sensors. Crucially, the results indicate that the large contact pressures, readily available in applications such as road-tyre contact and wave energy, alone could be enough to boost the performance, thus avoiding the need for costly surface engineering to increase A_r.

*Corresponding authors: Tel.: +44 141 3305653 and +44 141 3305136;
Daniel.Mulvihill@glasgow.ac.uk and Ravinder.Dahiya@glasgow.ac.uk

1. Introduction

Triboelectric nanogenerators (TENGs) are newly emerging renewable energy harvesters that rely on the triboelectric effect to convert mechanical energy to electrical energy. Repeated contact of surfaces having different electron affinities result in repeated cycles of charge transfer, and repeated generation of an electric field capable of driving an alternating current. Owning to their versatility, TENGs have been proposed for harnessing energy from a wide variety of mechanical sources including wave [1], wind [2], machine vibration [3] and human motion [4] for applications such as energy autonomous wearables [5-8] and portable personal entertainment devices [9]. Their combination of high efficiency at low frequency, light weight, portability, flexibility and low cost also make them unique among electricity generators. These attributes have made TENGs one of the most promising technologies for harnessing kinetic energy. However, one of the major limitations of TENGs has been their low power output (usually <<500 W/m^2 [10]). This is notwithstanding the large number of devices reported over last few years with the aim of boosting performance. Most of the focus has been on optimising the material selections [11] and engineering the contact surfaces [12, 13] and most of the work conducted to date has involved relatively low contact forces/pressures (such as with wearables). Output performance depends on a number of factors: materials, contact force, surface topography, frequency and separation distance. Surprisingly, the role of some of these aspects is still rather poorly characterised and understood in TENG design. In this paper, we investigate why TENG output increases with contact pressure. For the first time, we characterise both the electrical and contact area response for a TENG based on random rough surfaces in the high contact pressure regime as well as at low pressures. Surface roughness is known to effect aspects such as the frictional response of surfaces [14], the failure behaviour of materials [15] or the contact stiffness of interfaces [16], but here, we demonstrate how it governs the contact pressure versus electrical output of TENGs via its influence on the real contact area. The results lead to interesting implications including the ability to use large contact pressures to boost performance without the need for costly surface engineering. Several suitable high-pressure application areas are proposed for incorporating this approach with TENGs such as harnessing wheel-on-road contact for powering road infrastructure or vehicle electronic systems and generating large scale electricity from wave energy.

TENG electrical output is observed to be contact force dependent and generally increases as the force pressing the tribo-contact surfaces together increases [13, 17-22]. In few cases, the electrical output (e.g. open circuit voltage) shows linear variation with force [18, 19] and in others a later-stage saturation occurs at higher forces [13, 17, 20, 21]. What has not been clearly demonstrated, is the mechanism responsible for the contact force dependence. Here, we propose an explanation and then attempt to confirm this experimentally. Even the smoothest, nominally flat surfaces contain roughness

2

and we know from decades of research in the field of tribology that roughness gives rise to a force-dependent *real* contact area A_r [23, 24]. Generally, real contact area increases linearly with force at first (for low forces) and subsequently saturates in a non-linear fashion (at higher forces) as it approaches closer to the nominal contact area A_n. Now, assuming charge transfer in TENGs can only occur through areas of real contact, an increasing real contact area should generate an increasing total tribo-charge at the TENG interface. Therefore, because real contact area increases with contact force, so too should electrical output. Assuming that charge transfer is limited to areas of solid contact is a well-founded expectation because recent work [25, 26] has shown that contact electrification (via electron tunnelling) at an interface can only occur when the interatomic distance between atoms on either surface is within the equilibrium bond length (i.e. within the interatomic repulsive regime). A recent analytical model by the present authors in Xu *et al*. [27] has shown how accounting for a contact force-dependent real contact area (arising from random surface roughness) produces the commonly observed force-dependent TENG electrical performance, but this has yet to be explored experimentally until the present paper. Yang *et al*. [28] modelled the effect of different patterned surface types such as pyramids etc. (in contact with a flat surface) on the evolution of both contact area and electrical output (and included the effect of adhesion). The results predicted that both area and electrical output increase and later saturate as the surface pattern is flattened. Probably the most relevant experimental contribution to the question was contributed by Seol *et al*. [13], where the electrical output from a TENG interface consisting of a flat Ag surface in contact with a surface of PDMS pyramids is reported. Typical increase in the open circuit voltage, with load, up to the point of saturation was shown together with microscopic images of the PDMS pyramids in contact with a glass slide which qualitatively indicated a corresponding growth in contact area (i.e. size of the square contact patches). Interestingly, in a study on very similar patterned surfaces Seol *et al*. [22] identified hysteresis in the electrical output versus contact pressure plots upon loading and unloading. However, no quantitative experimental contact area measurements were plotted in any of these studies [13, 22, 28] and all are particular to idealised highly engineered (pyramid-on-flat) type contacts. Therefore, the role of contact area still remains to be demonstrated experimentally via measurement and calculation of real contact. Crucially, this kind of experimental study needs to be applied to the general class of non-engineered nominally flat rough surfaces (i.e. all non-patterned surfaces). This paper resolves this issue by accurately measuring *both* TENG electrical output and *real* contact area over a wide range of contact pressures (from first touch to heavily loaded) for two nominally flat rough surface tribo-contact pairs. All other parameters are fixed so that just the effect of the contact force can be elucidated. Fabrication and experimental setup are described in Section 2, results are discussed in Section 3 and key implications and applications of pressure dependence are addressed in Section 4.

2. Fabrication and Experiments

Device fabrication and surface characterisation is described in Section 2.1. Then two separate tests are described: one to measure TENG electrical output versus contact force (Section 2.2) and one to measure TENG real contact area versus contact force (Section 2.3).

2.1 TENG fabrication and surface characterisation

The device used for this study was a conductor-to-dielectric TENG in vertical contact separation mode. Fig. 1 shows a schematic. The TENG tribo-contact layers were copper sheet (100% Cu, thickness 50 μm) in contact with polyethylene terephthalate (PET) sheet (thickness 127 μm). The PET is coated with indium tin oxide (ITO) (resistivity 60 Ω/sq, thickness 0.130 μm, Sigma Aldrich, UK) to form the electrode on the PET side. Device dimensions (active tribo-contact surface) were 2.5 cm x 2.5 cm. Since the study is focused on the role of TENG *real* contact area, some additional measures were taken to ensure uniform contact conformity between the upper and lower tribo-contact layers. The upper and lower parts of the TENG were both fixed to optical glass plates (using double sided tape). Float glass plates possess both low flatness and low surface roughness (<0.05 μm). This measure is designed to eliminate any unwanted perturbances arising from substrate roughness and facilitate parallel contact of the tribo-layers. In addition, the lead wires were attached to the electrodes outside the active device area to avoid a bulge affecting the contact area.
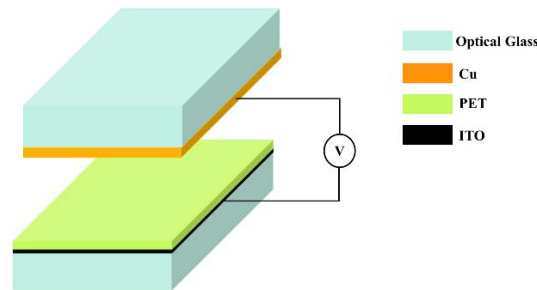

Fig. 1: Schematic of the contact separation mode TENG having copper (Cu) in contact with polyethylene terephthalate (PET).

The surface topography of both the Cu and PET surfaces was measured prior to testing (i.e. pristine surfaces were measured). The Cu surface was scanned using an optical 3D surface profilometer (Alicona InfiniteFocus) and the PET was scanned using an atomic force microscope (AFM) (Dimension Icon, Bruker). The roughness scans for both Cu and PET are shown in Fig. 2 and Table 1 reports center-line average roughness, Root Mean Square (RMS) roughness and RMS surface gradient (see Appendix A for explanation of these parameters). Note that the Cu surface is nearly three orders of magnitude rougher than the PET. PET film is transparent, and its root mean square (rms) roughness is in the nano-scale. These two factors make it nearly impossible for the optical profiler to determine accurate roughness measurements. Hence an AFM was used to measure the PET surface.
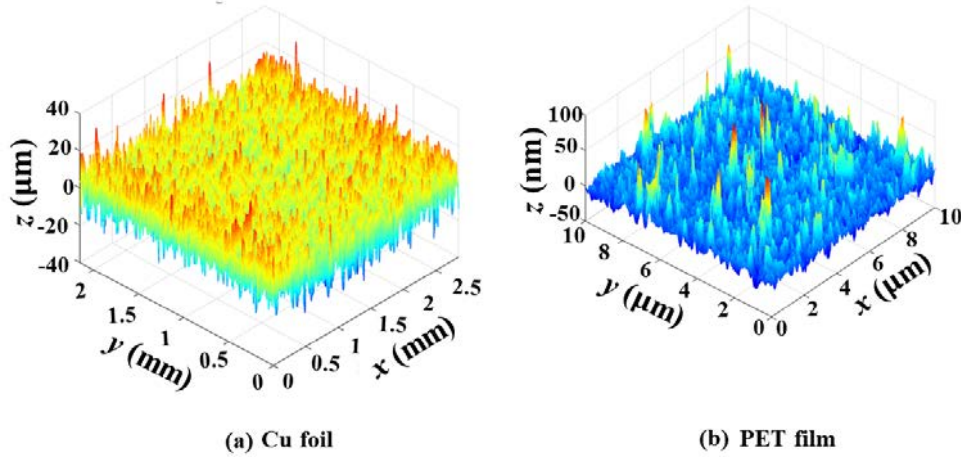
Figure 2: TENG surface topography (a) Cu foil and (b) PET film. Note: the *z*-axis is in micrometer for Cu and nanometer for PET due to the roughness difference.

Table 1: Areal surface topography parameters of TENG tribo-contact surfaces (see Appendix A for information on parameters used).

Contact material	Center line average (S_a) (μm)	RMS roughness (S_q) (μm)	RMS surface gradient
Cu foil	4.8	6.1	0.84
PET film	0.0067	0.0095	0.17

2.2 TENG Electrical measurements

The setup in Fig. 1 (TENG with glass backing plates) was then installed in a custom designed self-aligning test rig as shown in Fig 3a. Fig 3b shows the key detail via a sectional view. The device in Fig 1. (TENG (1) with glass backing plates (2)) is attached to upper and lower smooth ground metal platforms (3 and 4). Again, because our focus is on contact area, it is critical that the rig is designed to enable parallel contact of the upper and lower TENG tribo-contact surfaces. Indeed, Hong *et al*. [29] found that open circuit voltage dropped by nearly 75% in their study for a misalignment of only 1°. In our rig, rotation of the upper platform (3) is fixed, but the lower platform (4) is free to rotate on a spherical bearing ball (5). Prior to testing, a pre-load is applied to make contact and self-align the surfaces. The alignment is then 'locked-in' by tightening the lock screws (6). Mechanical oscillation was supplied at 0.5 Hz via a mechanical testing frame (Instron 3367, USA) for contact loads ranging from 20 to 930 N. Note, a low operation frequency ensures the load cell can correctly resolve the peak contact force. This is an important consideration since we are studying the effect of contact force. At high frequencies, it would be important to ensure a given load cell and data acquisition system has the temporal resolution to capture the peak contact force. A key element of the study to be able to characterise the force-dependent response over a sufficiency wide range of applied forces: specifically, from very low forces up to forces required for potential saturation of TENG electrical

5

output. Therefore, for low forces (2 to 10 N), mechanical oscillation was supplied by an electrodynamic shaker system (TIRA, TV 50018, Germany) with a 20 N load cell capacity. Separation distance was fixed at 2 mm and the open circuit voltage was recorded by an oscilloscope (MSO-X 4154A, KEYSIGHT, USA). The oscilloscope was connected with an operational amplifier and a voltage divider circuit (resistances of 1G Ω and 6G Ω) to ensure that the impedance of the voltage meter setup was much larger than the TENG internal impedance (See Fig. S1 for details). Details of the short circuit current measurement approach are given in the Supporting Information (see Fig. S2). Both tribo-contact surfaces were cleaned prior to testing (using acetone and isopropanol initially, then rinsing in RO water and finally blow dried using a nitrogen gun). During the test, the contact load was progressively increased and, at each load value, TENG open circuit voltage and short circuit current was measured after a TENG operation period of 250 cycles in order to ensure equilibrium of tribo-charge generation.
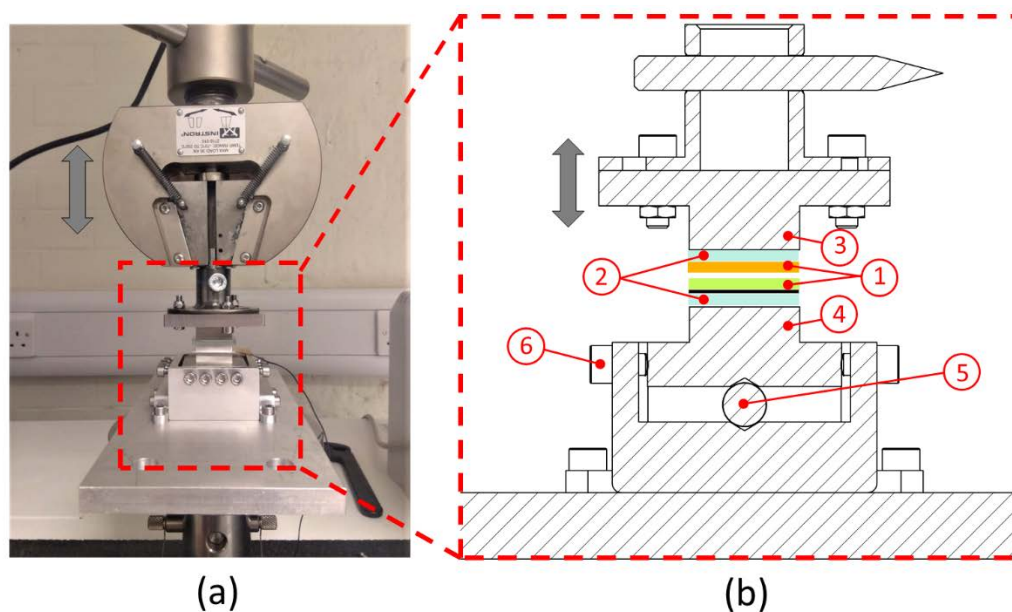

Fig. 3: TENG self-aligning test setup: (a) Photo of test rig in mechanical test machine and (b) Sectional view of the test rig. The numbered parts are (1) TENG device (Cu and PET), (2) Glass plates, (3) Upper rig platform, (4) Lower rig platform, (5) Spherical bearing ball and (6) Locking screws.

2.3 TENG Contact area measurements

Pressure sensitive film (SPF-A, Pressure Sensors Inc., USA) was used to determine the TENG real contact area. The contact area measurement technique is outlined schematically in Fig. 4. The film is placed between the TENG tribo-contact layers (Fig. 4a) and contact force is applied via the test rig (Fig. 4b). The pressure sensitive film consists of two PET layers: a donor layer and a receiver layer. Both donor and receiver films where cut to 3 cm x 3 cm (larger than the 2.5 cm x 2.5 cm TENG area to avoid edge effects). The donor film is coated with a thin layer of micro-capsules and a colour developing layer is coated onto the receiver. Once the *local* contact pressure exceeds a threshold value, the micro-

capsules at these locations break and the capsuled ink transfers to the receiver surface where it reacts with the developer layer to produce red spots in areas of contact (see Fig. 4c). A sample of a tested film is shown in Fig. 4d. The lateral resolution of the measurement (2.6 μm) is determined by the capsule size (specifications for the pressure sensitive film are given in [30]). Following testing, the film is scanned (with 1200 dpi resolution) to produce a digital image for analysis. A MATLAB code is then used to threshold the image to generate binary images and the total area of contact is calculated. The contact area test had to be carried out separately to the electrical measurement test (as the pressure sensitive film will grossly alter the electrical properties of the device). The surfaces were cleaned and aligned (for parallelism) prior to testing. Load was then increased monotonically up to the same load points as for the electrical measurements (i.e. there is no oscillation in the contact area test). At each load point, the pressure sensitive film is removed and a new one is inserted before proceeding to the next load point.
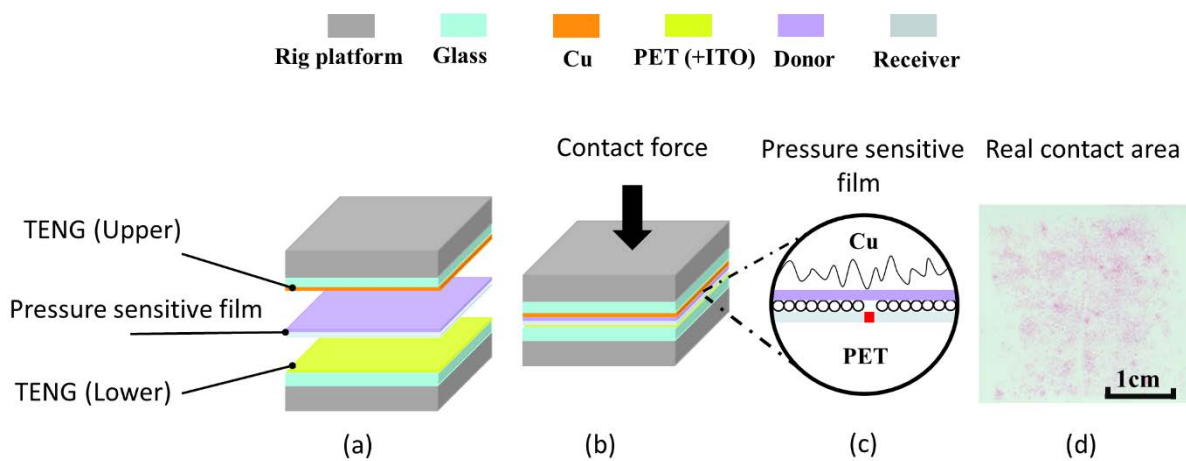

Fig. 4: Real contact area measurement using pressure sensitive film: (a) Pressure sensitive film sandwiched between tribo-layers, (b) Compression of layers under contact force, (c) Pressure sensitive film operation and (d) Sample tested film showing areas of contact in red/pink.

3. Results: Electrical output and contact area

Fig. 5a plots the TENG open circuit voltage signals used for device characterisation. A signal is shown for 12 contact forces between 20 and 930 N corresponding to nominal contact pressures of 32 to 1488 kPa. Note that, since the nominal contact area varies in the TENG literature, it is necessary to use nominal contact pressure (i.e. force/nominal area) to enable comparison. For a given contact force, the peak voltages in Fig. 5a are almost constant indicating equilibrium of TENG operation. The peak positive voltages are then taken from Fig. 5a and plotted (together with short circuit current) against contact pressure (and force) in Fig. 5b. In Fig. 5b, open circuit voltage increases with contact pressure and the upper end of the pressure range here is also sufficient to saturate the open circuit voltage: i.e. beyond about 1176 kPa (753 N), the voltage levels off at around 88 V. This is in-line with previous studies [13, 17, 20, 21] who have noted a similar response. Fig. 5b also indicates a very similar response

for short circuit current. What has not, so far, been elucidated very clearly is exactly why electrical output increases with contact pressure. To answer this question, we turn our attention to the real contact area at the interface.
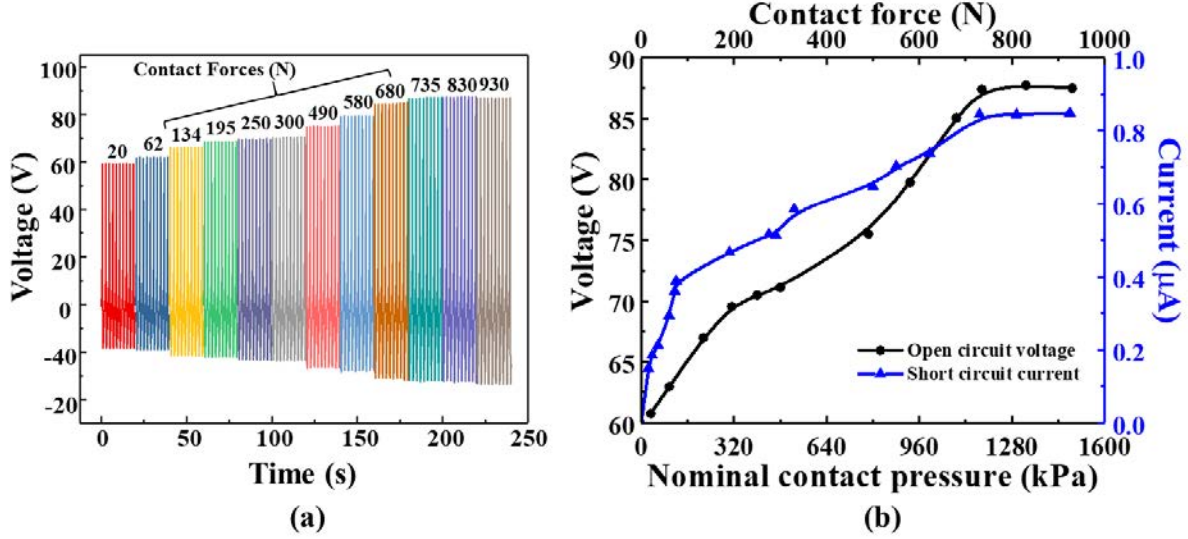

Fig. 5: (a) Sample of TENG open circuit voltage signals for increasing contact force and (b) Peak open circuit voltage and peak short circuit current versus nominal contact pressure (and force).

Fig. 6a shows a sample of the pressure sensitive film results for the 32 to 1488 kPa contact pressure range. The images on the left are the as-scanned images with the pink spots representing real contact at the TENG interface. The images on the right are the binary images with white representing real contact. The total real contact area A_r is simply the sum of the white areas and the contact area ratio is defined as (A_r/A_n) where A_n is the nominal device contact area of 2.5 x 2.5 = 6.25 cm^2. Note from Fig. 6a that contact is spread relatively evenly over the nominal area and not biased towards any particular edge or corner. This is a good indication that the careful measures taken to ensure parallelism of the tribo-contact surfaces in Section 2 (i.e. glass backing plates and self-aligning contact) have been successful. When the contact pressure is low (32 kPa case in Fig. 6a), only a few points evenly distributed over the nominal contact area are found to be in solid contact. As the pressure is increased, the area of solid contact grows. The pressure sensitive film result for the maximum contact pressure case in Fig. 6a (1488 kPa) is notably different to the 32 kPa result – here a rather large amount of area is in contact. The increase is quantified in Fig. 6b where contact area ratio is plotted against contact pressure. Notice just how small the real contact area is at low contact pressures: at 32 kPa, the contact area ratio is only 0.0029 (i.e. 0.29%) and, at 99 kPa, only 0.073 (i.e. 7.3%). This is important to bear in mind when we consider that the vast majority of published work on TENGs has been carried out at relatively low contact pressures. Table 2 compares the nominal contact pressure ranges used across a representative selection of studies on contact-separation mode TENGs (with both engineered

and non-engineered surface topographies). All of the previous studies in Table 2 were conducted at contact pressures below 200 kPa. This means that only the first two cases (32 & 99 kPa) in Fig. 6a are within this range and we can see from the pressure sensitive film that contact is still rather sparse at these pressures (for the material pair here). Indeed, many of the prevalent TENG applications are only capable of applying very small contact pressures (normal pressures in worn clothing are generally less than 10 kPa [31-33]) and, although reasonable to a tribologist, it is likely that the TENG community will not have been aware of just how little true contact area is generated under these pressures.

In this work, we go beyond the 0-200 kPa range depicted in Table 2 and characterise performance up to a contact pressure of 1488 kPa. To our knowledge, this is the first time a TENG has been characterised over such a wide pressure range covering both low and high pressures. Referring back to Fig. 6, we see that contact area grows approximately linearly in the lower pressure regime and then tapers off at higher pressures. Beyond about 1176 kPa (735 N), the contact area ratio saturates at about 0.82. This kind of general evolution of real contact area versus contact pressure has been well observed in the tribology literature [23, 24] and results essentially from the inevitable presence of roughness on even the smoothest fabricated surfaces (i.e. only the extreme peaks of the roughness make contact at first, more peaks then come into contact as the contact pressure is increased until the number of new contact patches and the real contact area saturates – see the roughness scans in Fig. 2). However, what is particularly interesting here is the comparison of the contact area measurement with the open circuit voltage and short circuit current measurement.
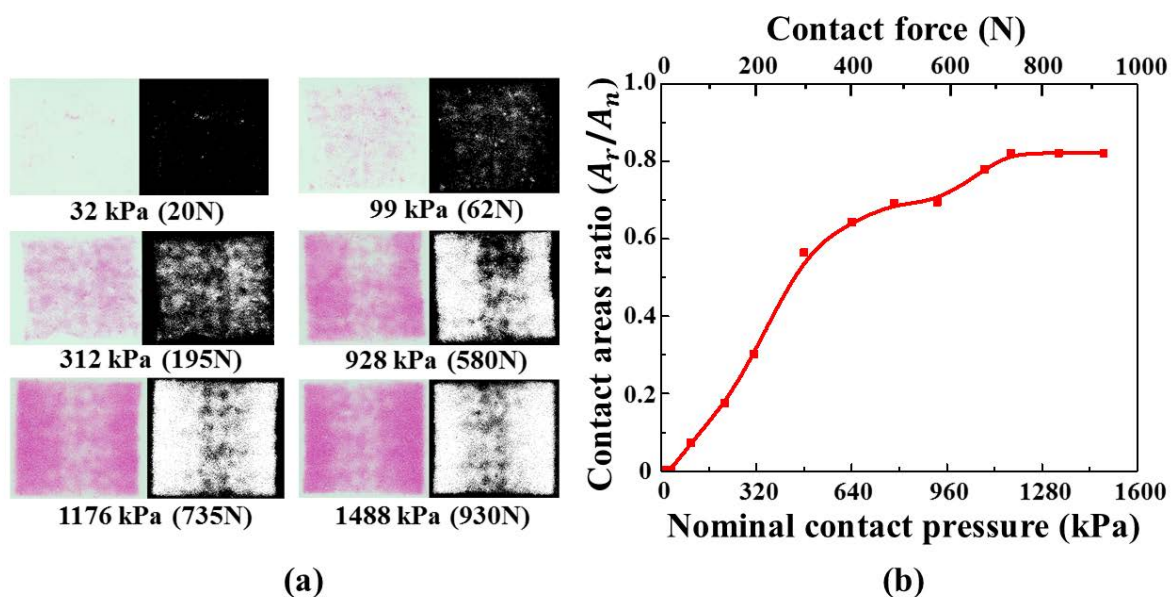

Fig. 6: (a) Real contact area as detected by pressure sensitive film with increasing contact pressure showing as-scanned film with pink indicating solid contact (left) and binarized image with white indicating solid contact (right) and (b) Contact area ratio (A_r/A_n) versus nominal contact pressure (and force). Note: the nominal contact patch size in (a) is 2.5 cm x 2.5 cm.

Table 2: Typical nominal contact pressures (force/area) used in TENG studies compared with the present work (final row).

Contact Materials	Surface topography	Contact force (N)	Nominal contact area (cm^2)	Nominal contact pressure (kPa)	Ref.
PDMS & Al/Ag CNF	Engineered	0.5 to 7	2.9	1.7 to 24	[17]
Ag & PDMS	Engineered	4 to 60	4.0	10 to 150	[13, 17]
Ag & PDMS	Engineered	200 to 700	36.0	56 to 194	[19]
PTFE & C-PUF	Engineered	1 to 12	36.0	0.3 to 3.3	[20]
Cu & PDMS	Engineered	18 to 90	9.0	20 to 90	[21]
Al & PDMS	Non-Engineered	40 to 220	25.0	16 to 88	[34]
Glass & PDMS	Non-Engineered	10 to 50	25.0	4 to 20	[35]
PET & PDMS	Non-Engineered	20	25.0	8	[36]
PI & Nylon	Non-Engineered	30 to 60	6.25	48 to 96	[37]
Al & PDMS	Non-Engineered	20 to 40	2.25	89 to 178	[38]
PET & PDMS	Non-Engineered	4.3 to 5.1	3.75	11 to 13.6	[18]
Al & PVDF	Non-Engineered	50	14.44	34.6	[39]
Cu & PET	Non-Engineered	2 to 930	6.25	3.2 to 1488	This work

Fig. 7a plots both open circuit voltage and contact area ratio against contact pressure in the same graph. The max open circuit voltage increases from 14.9 V to 87.5 V as the contact area ratio increases from 0.0025 to 0.82. What is particularly interesting are the similarities in form between the two curves. In particular, both open circuit voltage and contact area ratio saturate at about the same value of contact pressure (i.e. around 1176 kPa). A similar trend is seen in Fig. 7b for short circuit current. This essentially suggests that the electrical output is governed by the real contact area. To gain an insight into how this happens, we recall that the open circuit voltage V_{oc} for the device (parallel plat capacitor model) is given by:

$$V_{\mathrm{oc}} = \frac{Q_T x(t)}{A_n \varepsilon_o},$$

(1)

where, $x(t)$ is separation distance, ε_o is the permittivity of air and A_n is the nominal contact area. Now, since these parameters are constant in our experiment, we can conclude that the total tribo-charge Q_T is likely increasing with contact pressure. Assuming tribo-charges can only transfer through the real contact area A_r, and defining σ_T as the areal density of tribo-charge transfer through A_r, we can write:

$$Q_T = \sigma_T A_r$$

(2)

Taking σ_T as a constant for the material pair, Eqs (1) and (2) suggest why V_{oc} is dependent on real contact area. The assumption that tribo-charges can only transfer at areas of real contact is reasonable as it has been demonstrated in recent work [25, 26] that triboelectrification (via electron tunnelling) requires the interatomic distance between atoms across an interface to be within the equilibrium bond distance (i.e. within the repulsive regime). Also, because we are dealing with dielectric materials, this charge should remain localised in the real contact areas. We established in Fig. 6 that real contact area in the TENG is highly contact pressure dependent. Thus, taking these two pieces of information

together, it should follow that total tribocharge, and hence TENG electrical output, should be dependent on contact pressure via the real contact area. Indeed, as we have seen, the results in Fig. 7 strongly point in this direction as V_{oc} and I_{sc} appear to follow the evolution of real contact area with pressure. Eq. 2, of course, assumes that tribocharges are uniformly distributed and constant over areas of real contact. In fact, the distribution of charges within the real contact area is somewhat unknown and requires significant further study. However, a constant tribocharge density has generally been assumed in the literature and, in any case, even if it is not constant the σ_T in Eq. 2 can be considered as the net or equivalent value leading to the same total charge. The blue hatched regions in Fig. 7 encompasses the pressure range (0 to 200 kPa) from previous literature as depicted in Table 2. We can see that a much wider pressure range has been investigated in the present work revealing significant scope for increasing output at higher pressures. For example, at 200 kPa (the max pressure in Table 2), the contact area ratio is still less than 0.2, but it reaches 0.82 beyond about 1168 kPa. Note: we have observed gains of 5.8 and 4.9 for V_{OC} and I_{SC}, respectively as A_r was increased from 0.25 to 82%. It is difficult to compare this directly with the effect of other TENG parameters due to the variety of material pairs etc. used across the literature. However, to provide some indicative perspective: It is less than the gains of 50 and 8.5 reported in [36] for V_{OC} and I_{SC} as separation distance was varied from 0.1 to 1 mm. On the other hand, the V_{OC} gain of 5.8 is comparable with V_{OC} gains of 2.6 to 8 reported with changes in tribo-layer thickness (0.02 to 2 mm) in [40, 41], while the I_{SC} gain of 4.9 is of a similar order to I_{SC} gains of 2.4 to 6 reported with change in frequency (0.5 to 5 Hz) in [36, 42]. A detailed parametric study would be required to determine a rank order of the sensitivity of TENG output to the different parameters.
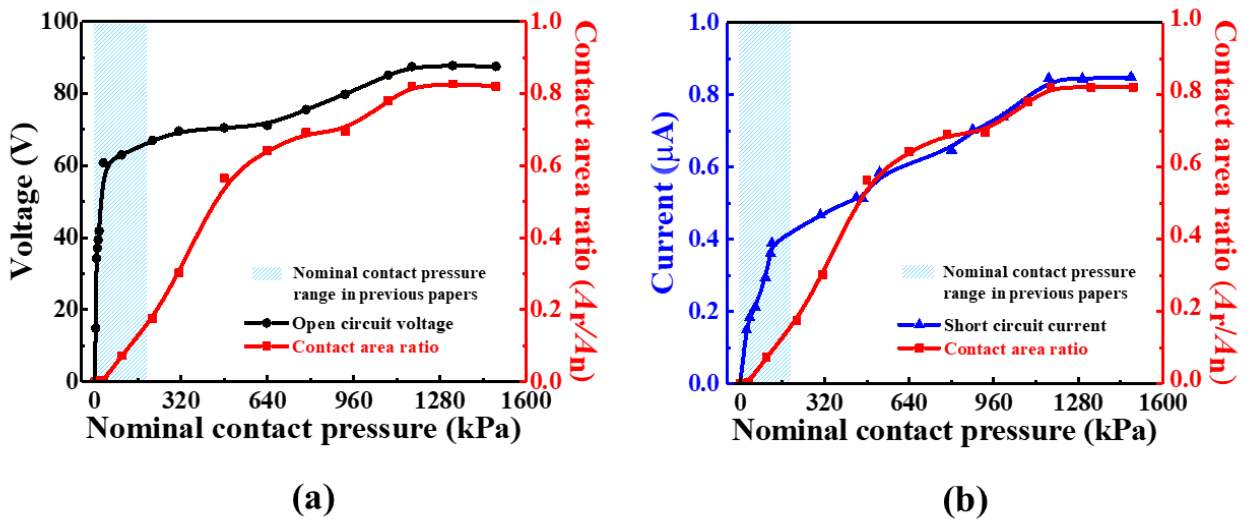

(a)   **(b)**

Fig. 7: (a) Open circuit voltage and contact area ratio (A_r/A_n) versus nominal contact pressure and (b) Short circuit current and contact area ratio (A_r/A_n) versus nominal contact pressure. The blue hatched regions represents the pressure range in previous literature (as depicted in Table 2).

To provide a visual demonstration of the effect of increasing the real contact area (via the contact pressure), 21 LEDs forming the word 'BEST' were connected in series with the TENG as the power source (Fig. 8b). Contact pressure was then increased in the same steps as before and LED performance was imaged via a digital camera at each step. Fig. 8a illustrates how the LEDs get progressively brighter as the contact pressure (and contact area ratio) increase. Contact pressure increases the real contact area meaning that total charge can increase: this increases voltage and current, and hence, the LEDs become progressively brighter until saturating at points 3 and 4 in Fig. 8a.
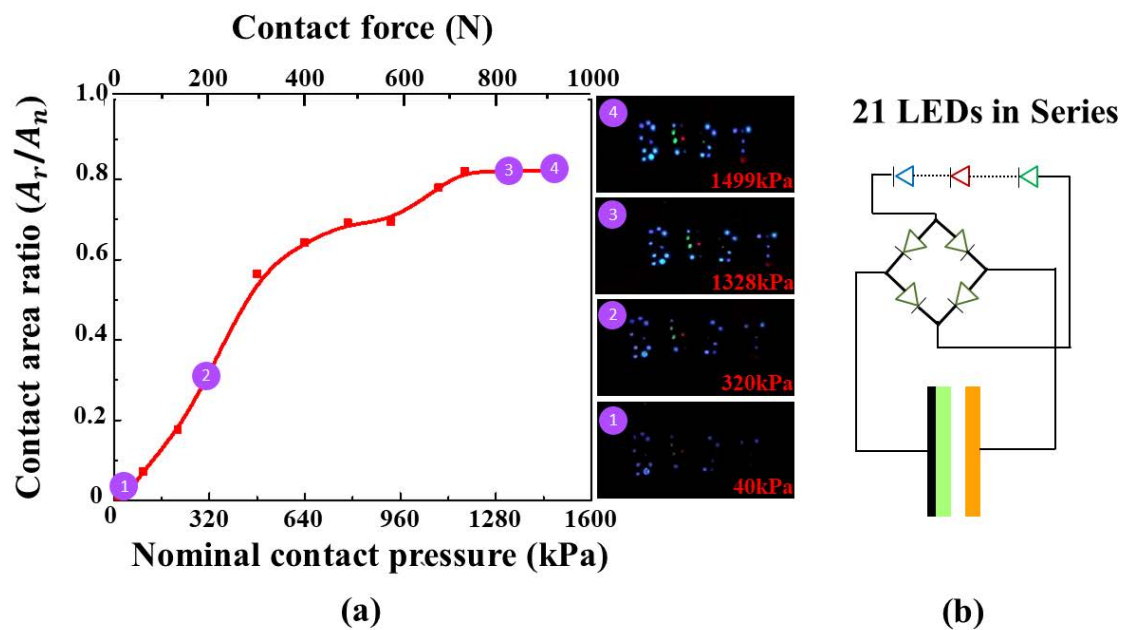

Fig. 8: (a) LED array performance versus nominal contact pressure and force (and contact area ratio) and (b) representative energy harvesting circuit. The LED array represents the word "BEST" – the LEDs become progressively brighter as the contact pressure (and contact area) is increased.

4. Implications and applications of pressure and area dependence

There are a number of important implications that follow from the idea that TENG electrical performance is dependent on a contact pressure-dependent real contact area. The first is that device designers need to carefully account for the real contact area dependence over the design range of contact pressures envisaged for a given device: failure to account for this is likely to result in inaccurate predictions of device performance. While the early TENG models [36, 43] did not account for contact pressure dependence, a recent model by the present authors [27] accounts for the effect by including the rough surface contact mechanics governing the behaviour in a unified TENG model. Material properties, surface topography and contact pressure all influence the real contact area and the model in Xu *et al*. [27] uses input from each to these to predict real contact area, and by extension, electrical output.

12

The continued boosting of TENG output at higher pressures characterised in the present work also indicates possible new application areas for TENGs – what we might call 'high pressure applications'. In fact, there are a number of sources of high-pressure cyclic loading in the world around us. Table 3 summarises the typical contact pressures available with a selection of these sources. A particularly suitable and abundant source is the vehicle wheel-on-surface interaction. For example, in trucks a contact pressure in excess of 1700 kPa is available at the tyre-road interface (Table 3). Here, TENGs positioned either in the tyre or on the road surface could be used to power a variety of sensors for integration with either the truck's electronic systems or the road infrastructure (e.g. traffic light sensors, warning lights etc.). Similar possibilities occur with automobiles, locomotives and construction & agriculture-based vehicles. Another suitable source is the repeating pressure available from sea waves. Here TENGs can be adapted to take advantage of the higher pressures available for the purpose of generating electricity. For example, pressures in excess of 100 kPa are available from wave interaction with a stationary surface and pressures of almost 9000 kPa have been observed for waves impacting a moving ship hull (Table 3).

Table 3: Typical contact pressures available in possible high load applications for TENGs.

High pressure application	Contact pressure range	Ref
Truck tire vs road	344 to 1723 kPa (range in central 8 cm)	[44]
Locomotive wheel vs rail	700 to 1600 MPa (Peak), 117 to 1167 MPa (Mean)	[45]
Automobile tire vs road	172 to 275 kPa (mean)	[46]
Wave vs tilted slope (1:4)	50 kPa (mean pressure at max peak wave loading)	[47]
Wave vs offshore vertical wall	110 kPa (mean pressure at max peak wave loading)	[48]
Wave vs moving ship hull ('slamming')	2068 to 8963 kPa (mean pressure at peak wave loading)	[49, 50]

Previous literature has focused on boosting TENG output by developing highly engineered surface topographies. Indeed, the present work helps to explain why so many authors [12, 21, 39, 51-53] have noted improvements in TENG performance based on modifications to surface topography – i.e. they were most likely increasing the real contact area. An interesting point to add to this is that, achieving a contact area ratio greater than unity is possible – imagine a hard-sawtooth type surface in contact with a soft counter-surface. The sawtooth surface clearly has an area greater than the nominal area and this can become the interfacial contact area when pressed into a sufficiently soft counter-surface. However, the present paper demonstrates that we can also boost TENG performance with simple non-engineered surfaces. In applications where sufficient pressure is available (Table 3), this is a far more

cost-effective route. Where contact pressure is limited, softer materials can be easily be chosen so that contact area saturation occurs at lower pressures.

Another important implication relates to the definition and measurement of tribo-charge density. The fact that A_r is generally less than A_n (and especially so at low contact pressures) highlights an important distinction between the tribo-charge density as defined in Eq. (2) (i.e. Q_T/A_r) and the conventional definition as Q_T/A_n. It means that tribo-charge density defined as Q_T/A_n cannot be considered to be a fixed quantity (for a material pair), but will depend on the contact pressure and even the surface roughness (via the Q_T generated by the real contact area which is both pressure and roughness dependent). Therefore, there is a need for clarity in the measurement of tribo-charge density essentially to account for the important distinction between the contact pressure dependent A_r and the nominal device area A_n. Current literature does not account for this and there is, therefore, a strong need for further research focused on the measurement of tribo-charge density. Another important consideration here might be whether the interface materials are insulators or conductors. While tribo-charges will remain localised at areas of solid contact for dielectric materials, tribo-charges for a conductor (i.e. in a conductor-to-dielectric TENG) can be expected to distribute over the entire nominal device area. Yet another consideration is how the distribution of real contact area effects output – i.e. would identical real contact areas with differing spatial distribution produce similar electrical output? This question also requires further attention.

Finally, the results demonstrated in Section 3 mean that TENGs can be used as effective load and pressure sensors. A careful calibration of output voltage or current versus contact force (and operation within the elastic regime) is essentially all that would be required for a TENG system to report loads and/or pressures. Example applications include pressure/force measurement in vehicle weigh stations, road tyres, shoes and at contact interfaces in vibrating machinery.

5. Conclusions

This paper has investigated the origin of the contact force-dependent performance of TENGs. Experiments were carried out where open circuit voltage and short circuit current were measured together with real contact area under increasing contact force/pressure with identical test conditions for a TENG involving two nominally flat surfaces (PET and Cu) in contact separation mode. Digitised pressure sensitive film was used to directly measure the real contact area – to the authors knowledge, this is the first-time both real contact area and electrical output have been measured between two nominally flat surfaces in a TENG device. Special precautions such as ultra-flat backing plates and a self-alignment facility were shown to ensure the required contact conformity at the interface. Results show that open circuit voltage, short circuit current and real contact area all increase with contact

pressure. For low contact pressures, the amount of real contact area is tiny. For example, at 16 kPa (10 N on 25 x 25 mm^2) the percentage of real contact was only 0.25% of the active device area. Voltage, current and contact area increase roughly linearly at first and later saturate to a converged value at higher contact pressures. Real contact area at saturation (beyond about 1168 kPa) was about 82% - this represents an enormous increase in contact area over the pressure range investigated. Critically, both open circuit voltage and short circuit current saturated at almost the same contact pressure as the real contact area suggesting that electrical output follows the evolution of the real contact area. Recourse to simple TENG theory reveals that, since the key TENG parameters (maximum separation distance, material properties etc.) where constant during the experiment, the total tribo-charge at the interface must have been increasing with contact pressure. The most likely explanation; therefore, is that tribo-charges require real (or solid) contact in order to transfer at an interface (a valid assumption given that recent work [25, 26] suggests that triboelectrification can only occur for atom pairs within the equilibrium interatomic bond distance). Therefore, an increasing total tribo-charge (and hence electrical output) is to be expected if real contact area increases with contact pressure. The reason why real contact area increases with contact pressure is simply because nominally flat surfaces, however smooth, inevitably contain random multi-scale surface roughness and the mechanics of rough surface contact essentially leads to a contact pressure-dependent contact area (see Xu *et al*. [27]). Material properties, surface topography and contact pressure all influence the contact area response.

There are several implications of these observations for TENGs. The first is that TENG designers will need to account for pressure dependence over the design range of contact pressures experienced by a device – otherwise predictions of output performance may be inaccurate. This is especially important as most TENG devices operate in the low contact pressure regime where contact area (as we see here) can be a surprisingly small fraction of the nominal area even for very smooth surfaces (and is also very sensitive to contact pressure in this regime). The paper also essentially explains why so many authors have been able to boost TENG performance by designing novel surface topographies – in most instances, the increase in output is likely due to an increase in real contact area. The distinction between real and nominal contact area leads to another important point relating to tribo-charge density and its measurement. There now needs to be clarity on whether tribo-charge density is calculated based on the real contact area or the nominal active device area and the approach needs to be justifiable for a given application. Pressure-dependence also means that (after a simple calibration) TENGs can be used as force and pressure sensors (e.g. pressure/force measurement in vehicle weigh stations, road tyres, shoes or even at contact interfaces in vibrating machinery). Finally, unlike in previous studies, the work characterises the increasing TENG output well into the high

contact pressure regime (up to 1488 kPa). This leads to the ability to use large contact pressures to boost performance without the need for costly surface engineering. Several readily available high-pressure application areas are proposed for incorporating this approach with TENGs such as harnessing wheel-on-road contact for powering road infrastructure or vehicle electronic systems and generating large scale electricity from wave energy.

Acknowledgments

Appendix A: Surface Roughness Metrology

The definitions, as well as the computing methods, of the metrology parameters used in Table. 1 are given here. All of these parameters are easily calculated from surface *x, y, z* data obtained from surface profilometers at sufficient resolution.

The roughness height, h, is leveled so that mean$(h) = 0$.

- Center line average (CLA) S_a:

$$S_a = \sqrt{|h|} = \sqrt{\frac{1}{n_x n_y} \sum_{i=1}^{n_x} \sum_{j=1}^{n_y} |h_{ij}|}$$

- Root mean square (RMS) roughness S_q:

$$S_q = \sqrt{\langle |h|^2 \rangle} = \sqrt{\frac{1}{n_x n_y} \sum_{i=1}^{n_x} \sum_{j=1}^{n_y} h_{ij}^2}$$

- RMS surface gradient S_{dq}:

A continuous form of RMS surface gradient is

$$\sqrt{\langle |\nabla h|^2 \rangle} = \sqrt{\langle \left(\frac{\partial h}{\partial x} + \frac{\partial h}{\partial y}\right)^2 \rangle} \approx \sqrt{\frac{1}{(n_x - 2)(n_y - 2)} \sum_{i=2}^{n_x-1} \sum_{j=2}^{n_y-1} \left[\left(\frac{\partial h}{\partial x}\right)_{ij}^2 + \left(\frac{\partial h}{\partial y}\right)_{ij}^2\right]^2}$$

where the partial derivatives are calculated using central differential scheme:

$$\left(\frac{\partial h}{\partial x}\right)_{ij} = \frac{h_{i+1,j} - h_{i-1,j}}{2\Delta_x}, \left(\frac{\partial h}{\partial y}\right)_{ij} = \frac{h_{i,j+1} - h_{i,j-1}}{2\Delta_y}$$

where Δ_x and Δ_y are the sampling resolution in the x and y directions, respectively.

References

[1] Chen, J., Yang, J., Li, Z., Fan, X., Zi, Y., Jing, Q., Guo, H., Wen, Z., Pradel, K. C., Niu, S., and Wang, Z. L., 2015, "Networks of Triboelectric Nanogenerators for Harvesting Water Wave Energy: A Potential Approach toward Blue Energy," ACS Nano, 9(3), pp. 3324-3331.

[2] Zhang, L., Zhang, B., Chen, J., Jin, L., Deng, W., Tang, J., Zhang, H., Pan, H., Zhu, M., Yang, W., and Wang, Z. L., 2016, "Lawn Structured Triboelectric Nanogenerators for Scavenging Sweeping Wind Energy on Rooftops," Advanced Materials, 28(8), pp. 1650-1656.

[3] Yang, W., Chen, J., Zhu, G., Wen, X., Bai, P., Su, Y., Lin, Y., and Wang, Z., 2013, "Harvesting vibration energy by a triple-cantilever based triboelectric nanogenerator," Nano Research, 6(12), pp. 880-886.

[4] Bai, P., Zhu, G., Lin, Z.-H., Jing, Q., Chen, J., Zhang, G., Ma, J., and Wang, Z. L., 2013, "Integrated Multilayered Triboelectric Nanogenerator for Harvesting Biomechanical Energy from Human Motions," ACS Nano, 7(4), pp. 3713-3719.

[5] Yi, F., Zhang, Z., Kang, Z., Liao, Q., and Zhang, Y., 2019, "Recent Advances in Triboelectric Nanogenerator-Based Health Monitoring," Advanced Functional Materials, 29(41), p. 1808849.

[6] García Núñez, C., Manjakkal, L., and Dahiya, R., 2019, "Energy autonomous electronic skin," npj Flexible Electronics, 3(1), p. 1.

[7] Dahiya, R., Yogeswaran, N., Liu, F., Manjakkal, L., Burdet, E., Hayward, V., and Jörntell, H., 2019, "Large-Area Soft e-Skin: The Challenges Beyond Sensor Designs," Proceedings of the IEEE, 107(10), pp. 2016-2033.

[8] Manjakkal, L., Pullanchiyodan, A., Yogeswaran, N., Hosseini, E. S., and Dahiya, R., 2020, "A Wearable Supercapacitor Based on Conductive PEDOT:PSS-Coated Cloth and a Sweat Electrolyte," Advanced Materials, 32(24), p. 1907254.

[9] Choi, A. Y., Lee, C. J., Park, J., Kim, D., and Kim, Y. T., 2017, "Corrugated textile based triboelectric generator for wearable energy harvesting," Scientific reports, 7(1), pp. 1-6.

[10] Zhu, G., Zhou, Y. S., Bai, P., Meng, X. S., Jing, Q., Chen, J., and Wang, Z. L., 2014, "A Shape-Adaptive Thin-Film-Based Approach for 50% High-Efficiency Energy Generation Through Micro-Grating Sliding Electrification," Advanced Materials, 26(23), pp. 3788-3796.

[11] Min, G., Manjakkal, L., Mulvihill, D. M., and Dahiya, R. S., 2020, "Triboelectric Nanogenerator With Enhanced Performance via an Optimized Low Permittivity Substrate," IEEE Sensors Journal, 20(13), pp. 6856-6862.

[12] Park, S.-J., Seol, M.-L., Jeon, S.-B., Kim, D., Lee, D., and Choi, Y.-K., 2015, "Surface Engineering of Triboelectric Nanogenerator with an Electrodeposited Gold Nanoflower Structure," Scientific Reports, 5(1), p. 13866.

[13] Seol, M.-L., Lee, S.-H., Han, J.-W., Kim, D., Cho, G.-H., and Choi, Y.-K., 2015, "Impact of contact pressure on output voltage of triboelectric nanogenerator based on deformation of interfacial structures," Nano Energy, 17, pp. 63-71.

[14] Mulvihill, D. M., and Sutcliffe, M. P. F., 2017, "Effect of tool surface topography on friction with carbon fibre tows for composite fabric forming," Composites Part A: Applied Science and Manufacturing, 93, pp. 199-206.

[15] Sneddon, S., Xu, Y., Dixon, M., Rugg, D., Li, P., and Mulvihill, D. M., 2020, "Sensitivity of material failure to surface roughness: a study on titanium alloys Ti64 and Ti407," Materials & Design, p. 109438.

[16] Mulvihill, D. M., Brunskill, H., Kartal, M. E., Dwyer-Joyce, R. S., and Nowell, D., 2013, "A Comparison of Contact Stiffness Measurements Obtained by the Digital Image Correlation and Ultrasound Techniques," Experimental Mechanics, 53(7), pp. 1245-1263.

[17] Uddin, A. S. M. I., Kumar, P. S., Hassan, K., and Kim, H. C., 2018, "Enhanced sensing performance of bimetallic Al/Ag-CNF network and porous PDMS-based triboelectric acetylene gas sensors in a high humidity atmosphere," Sensors and Actuators B: Chemical, 258, pp. 857-869.

[18] Vasandani, P., Mao, Z.-H., Jia, W., and Sun, M., 2017, "Relationship between triboelectric charge and contact force for two triboelectric layers," Journal of Electrostatics, 90, pp. 147-152.

[19] Song, J., Gao, L., Tao, X., and Li, L., 2018, "Ultra-Flexible and Large-Area Textile-Based Triboelectric Nanogenerators with a Sandpaper-Induced Surface Microstructure," Materials (Basel), 11(11), p. 2120.

[20] Zhang, H., Lu, Y., Ghaffarinejad, A., and Basset, P., 2018, "Progressive contact-separate triboelectric nanogenerator based on conductive polyurethane foam regulated with a Bennet doubler conditioning circuit," Nano Energy, 51, pp. 10-18.

[21] Zhang, X.-W., Li, G.-Z., Wang, G.-G., Tian, J.-L., Liu, Y.-L., Ye, D.-M., Liu, Z., Zhang, H.-Y., and Han, J.-C., 2018, "High-Performance Triboelectric Nanogenerator with Double-Surface Shape-Complementary Microstructures Prepared by Using Simple Sandpaper Templates," ACS Sustainable Chemistry & Engineering, 6(2), pp. 2283-2291.

[22] Seol, M.-L., Han, J.-W., Moon, D.-I., and Meyyappan, M., 2017, "Hysteretic behavior of contact force response in triboelectric nanogenerator," Nano Energy, 32, pp. 408-413.

[23] Müser, M. H., Dapp, W. B., Bugnicourt, R., Sainsot, P., Lesaffre, N., Lubrecht, T. A., Persson, B. N. J., Harris, K., Bennett, A., Schulze, K., Rohde, S., Ifju, P., Sawyer, W. G., Angelini, T., Ashtari Esfahani, H., Kadkhodaei, M., Akbarzadeh, S., Wu, J.-J., Vorlaufer, G., Vernes, A., Solhjoo, S., Vakis, A. I., Jackson, R. L., Xu, Y., Streator, J., Rostami, A., Dini, D., Medina, S., Carbone, G., Bottiglione, F., Afferrante, L., Monti, J., Pastewka, L., Robbins, M. O., and Greenwood, J. A., 2017, "Meeting the Contact-Mechanics Challenge," Tribology Letters, 65(4), p. 118.

[24] Helseth, L. E., 2017, "Optical force sensing principle based on transparent elastomer with a rough surface," Sensors and Actuators A: Physical, 263, pp. 667-676.

[25] Li, S., Zhou, Y., Zi, Y., Zhang, G., and Wang, Z. L., 2016, "Excluding Contact Electrification in Surface Potential Measurement Using Kelvin Probe Force Microscopy," ACS Nano, 10(2), pp. 2528-2535.

[26] Wang, Z. L., and Wang, A. C., 2019, "On the origin of contact-electrification," Materials Today, 30, pp. 34-51.

[27] Xu, Y., Min, G., Gadegaard, N., Dahiya, R., and Mulvihill, D. M., 2020, "A Unified Contact Force-Dependent Model for Triboelectric Nanogenerators Accounting for Surface Roughness," Nano Energy.

[28] Yang, W., Wang, X., Li, H., Wu, J., and Hu, Y., 2018, "Comprehensive contact analysis for vertical-contact-mode triboelectric nanogenerators with micro-/nano-textured surfaces," Nano Energy, 51, pp. 241-249.

[29] Hong, D., Choi, Y.-M., and Jeong, J., 2018, "Test bed for contact-mode triboelectric nanogenerator," Review of Scientific Instruments, 89(6), p. 065110.

[30] Surface Profiler Film, Sensor Products Inc, USA (https://www.sensorprod.com/surface-profiler-film/) [accessed 29/05/2020]

[31] Xiong, Y., and Tao, X., 2018, "Compression Garments for Medical Therapy and Sports," Polymers (Basel), 10(6), p. 663.

[32] Das, A., and Alagirusamy, R., 2010, "8 - Garment fit and comfort," Science in Clothing Comfort, A. Das, and R. Alagirusamy, eds., Woodhead Publishing India, pp. 159-172.

[33] You, F., Wang, J. M., Luo, X. N., Li, Y., and Zhang, X., 2002, "Garment's pressure sensation (1): subjective assessment and predictability for the sensation," International Journal of Clothing Science and Technology, 14(5), pp. 307-316.

[34] Ding, X., Cao, H., Zhang, X., Li, M., and Liu, Y., 2018, "Large Scale Triboelectric Nanogenerator and Self-Powered Flexible Sensor for Human Sleep Monitoring," Sensors (Basel), 18(6), p. 1713.

[35] Chen, J., Guo, H., Ding, P., Pan, R., Wang, W., Xuan, W., Wang, X., Jin, H., Dong, S., and Luo, J., 2016, "Transparent triboelectric generators based on glass and polydimethylsiloxane," Nano Energy, 30, pp. 235-241.

[36] Dharmasena, R. D. I. G., Jayawardena, K. D. G. I., Mills, C. A., Deane, J. H. B., Anguita, J. V., Dorey, R. A., and Silva, S. R. P., 2017, "Triboelectric nanogenerators: providing a fundamental framework," Energy & Environmental Science, 10(8), pp. 1801-1811.

[37] Saadatania, Z., Mosanenzadeh, S. G., Esmailzadeh, E., and Naguib, H., 2018, Performance-enhanced triboelectric nanogenerator using polyimide aerogel for energy harvesting and sensing, SPIE.

[38] Peng, J., Zhang, H., Zheng, Q., Clemons, C. M., Sabo, R. C., Gong, S., Ma, Z., and Turng, L.-S., 2017, "A composite generator film impregnated with cellulose nanocrystals for enhanced triboelectric performance," Nanoscale, 9(4), pp. 1428-1433.

[39] Bai, P., Zhu, G., Zhou, Y. S., Wang, S., Ma, J., Zhang, G., and Wang, Z. L., 2014, "Dipole-moment-induced effect on contact electrification for triboelectric nanogenerators," Nano Research, 7(7), pp. 990-997.

[40] Tao, X., Jin, H., Ma, M., Quan, L., Chen, J., Dong, S., Zhang, H., Lv, C., Fu, Y., and Luo, J., 2019, "Significantly Enhanced Performance of Triboelectric Nanogenerator by Incorporating BaTiO3 Nanoparticles in Poly(vinylidene fluoride) Film," 216(7), p. 1900068.

[41] Wang, Z., Liu, W., Hu, J., He, W., Yang, H., Ling, C., Xi, Y., Wang, X., Liu, A., and Hu, C., 2020, "Two voltages in contact-separation triboelectric nanogenerator: From asymmetry to symmetry for maximum output," Nano Energy, 69, p. 104452.

[42] Ahmed, A., Hassan, I., Helal, A. S., Sencadas, V., Radhi, A., Jeong, C. K., and El-Kady, M. F., 2020, "Triboelectric Nanogenerator versus Piezoelectric Generator at Low Frequency (<4 Hz): A Quantitative Comparison," iScience, 23(7), p. 101286.

[43] Niu, S., Wang, S., Lin, L., Liu, Y., Zhou, Y. S., Hu, Y., and Wang, Z. L., 2013, "Theoretical study of contact-mode triboelectric nanogenerators as an effective power source," Energy & Environmental Science, 6(12), pp. 3576-3583.

[44] Chen H.H., Connell R.B., Hudson W.R., Lytton R.L., Marshek R.M., Middleton D., Roberts F.L., Sarak C.L. and Tielking J.T. (1987) "Efffects of truck tire pressures on pavements", Research Study 372/386, Texas Transportation Institute, Texas A&M University, Texas USA.

[45] Zhou, L., Brunskill, H., Pletz, M., Daves, W., Scheriau, S., and Lewis, R., 2019, "Real-Time Measurement of Dynamic Wheel-Rail Contacts Using Ultrasonic Reflectometry," Journal of Tribology, 141(6).

[46] Rose, J.G. and Guenther T.E. (2009) "Vehicle tire-pavement interfacial surface pressure measurements and assesments", Research Report KTC-09-08, Kentucky Transportation Center, University of Kentucky, USA.

[47] Führböter, A., 1986, "Model and prototype tests for wave impact and run-up on a uniform 1:4 slope," Coastal Engineering, 10(1), pp. 49-84.

[48] Kisacik, D., 2012, "Loading conditions due to violent wave impacts on coastal structures with cantilever surfaces," PhD Dissertation, Gent University, Belguim.

[49] Henry, J. R., and Bailey, F. C., 1970, "Slamming of Ships: A Critical review of the current state of knowledge", Technical Report SSC-208, Ship Structure Committee, Washington D.C., USA.

[50] Daidola, J., and Mishkevich, V., 1995, "Hydrodynamic Impact on Displacement Ship Hulls. An Assessment of the State of the Art" Technical Report SSC-385, Ship Structure Committee, Washington D.C., USA.

[51] Yang, J.-H., Kim, Y.-K., and Lee, J. Y., 2015, "Simplified Process for Manufacturing Macroscale Patterns to Enhance Voltage Generation by a Triboelectric Generator," Energies, 8(11), pp. 12729-12740.

[52] Cheng, G.-G., Jiang, S.-Y., Li, K., Zhang, Z.-Q., Wang, Y., Yuan, N.-Y., Ding, J.-N., and Zhang, W., 2017, "Effect of argon plasma treatment on the output performance of triboelectric nanogenerator," Applied Surface Science, 412, pp. 350-356.

[53] Jeong, C. K., Baek, K. M., Niu, S., Nam, T. W., Hur, Y. H., Park, D. Y., Hwang, G.-T., Byun, M., Wang, Z. L., Jung, Y. S., and Lee, K. J., 2014, "Topographically-Designed Triboelectric Nanogenerator via Block Copolymer Self-Assembly," Nano Letters, 14(12), pp. 7031-7038.